Enhanced charge carrier mobility and lifetime suppress hysteresis and improve efficiency in planar perovskite solar cells

Energy & Environmental Science

Accepted Manuscript

This article can be cited before page numbers have been issued, to do this please use: S. H. Turren Cruz, M. Saliba, M. T. Mayer, H. Juarez Santiesteban, X. Mathew, L. Nienhaus, W. Tress, M. P. Erodici, M. Sher, M. G. Bawendi, M. Grätzel, A. Abate, A. Hagfeldt and J. Correa-Baena, *Energy Environ. Sci.*, 2017, DOI: 10.1039/C7EE02901B.

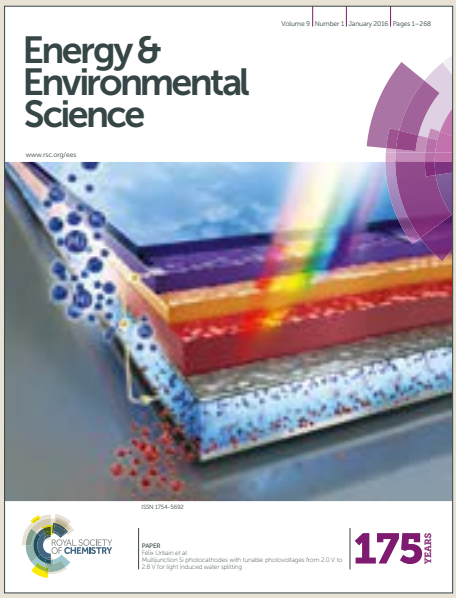

ROYAL SOCIETY OF CHEMISTRY

rsc.li/ees

View Article Online
DOI: 10.1039/C7EE02901B

Enhanced charge carrier mobility and lifetime suppress hysteresis and improve efficiency in planar perovskite solar cells

Silver-Hamill Turren-Cruz[1,2], Michael Saliba[1], Matthew T. Mayer[1], Hector Juárez-Santiesteban[2], Xavier Mathew[3], Lea Nienhaus[4], Wolfgang Tress[1], Matthew P. Erodici[5], Meng-Ju Sher[5], Moungi G. Bawendi[4], Michael Grätzel[1], Antonio Abate[6], Anders Hagfeldt[1]* and Juan-Pablo Correa-Baena[1,4]**

[1] École Polytechnique Fédérale de Lausanne, Station 6, CH-1015-Lausanne, Switzerland

[2] Benemérita Universidad Autónoma de Puebla. CIDS, Av. San Claudio y 18 Sur, Col. San Manuel, Ciudad Universitaria, CP 72570, P.O. Box 1067, Puebla, Pue., 7200, México

[3] Instituto de Energías Renovables, Universidad Nacional Autónoma de México, Temixco, Morelos 62580, México

[4]Massachusetts Institute of Technology, Cambridge, MA 02139

[5]Wesleyan University, Middletown, CT, 06459

[6]Young Investigator Group Active Materials and interfaces for stable perovskite solar cells, Helmholtz-Zentrum Berlin für Materialien und Energie, Kekuléstrasse 5, 12489 Berlin, Germany

*Corresponding authors: MS Michael.saliba@epfl.ch; AH anders.hagfeldt@epfl.ch; JPCB jpcorrea@mit.edu

Keywords: Planar perovskite solar cell, photovoltaics, morphology, perovskite crystals, open-circuit voltage, THz spectroscopy, mobility in perovskites, hysteresis.

View Article Online
DOI: 10.1039/C7EE02901B

Abstract

Perovskite solar cells (PSCs) are very promising lab-scale technologies to deliver inexpensive solar electricity. Low-temperature, planar PSCs are of particularly interest for large-scale deployment due to their inherent suitability for flexible substrates and potential for silicon/perovskite tandems. So far, planar PSCs have been prone to large current-voltage hysteresis and low stabilized power output due to a number of issues associated with this kind of device configuration. We find that the suppression of the yellow-phase impurity (∂-$FAPbI_3$) present in formamidium-based perovskites, by RbI addition, contributes to low hysteresis, higher charge carrier mobility, long-lived carrier lifetimes and a champion stabilized power output of 20.3% using SnO_X as the electron selective contact. We study the effects of these impurities on the transient behavior that defines hysteresis and its relation to ionic movement. In addition, we find that the formation of a $RbPbI_3$ phase does not significantly affect the charge carrier lifetimes and consequently the performance of the devices. This brings new physical insights onto the role of different impurities in perovskite solar cells, which make these materials so remarkable.

View Article Online
DOI: 10.1039/C7EE02901B

Introduction

In the last few years organic-inorganic hybrid perovskite solar cells (PSCs) have emerged as one of the most promising candidates for thin-film, low cost solar technologies.(*1*) Perovskites used for photovoltaics (PV) have an AMX_3 formula that is comprised of a monovalent cation, A = cesium (Cs^+), methylammonium (MA); formamidinium (FA);(*2-7*) a divalent metal M = (Pb^{2+}; Sn^{2+})(*8-10*); and a halide anion X = (Cl^-, Br^-; I^-).(*11*)

These materials exhibit high optical absorption coefficients(*12*) and long charge carrier diffusion lengths in the μm-range. (*13, 14*) These properties have allowed the power conversion efficiency (PCE) of PSCs to jump from 3.8%(*15*) in 2009 to 22.1%(*16, 17*) in 2016, which is unprecedented for any other PV material.(*18, 19*) Much excitement is also due to the possibility of processing perovskite materials by a large number of techniques ranging from spin coating,(*8*) dip coating,(*20*) 2-step interdiffusion,(*21*) and vacuum assisted evaporation.(*22*) Most of these techniques are low temperature compatible (<100 °C) and can be solution-based. Therefore, PSCs are ideal for low-cost commercialization.

The highest reported efficiencies have been achieved with perovskites with mixed MA/FA cations and Br/I halides(*4, 23*). Recently, Cs was used to explore more complex cation combinations, i.e. Cs/MA, Cs/FA and Cs/MA/FA(*7, 24-27*). Similarly, Rb was added into a multication perovskite, showing improved efficiency and long-term device stability at elevated temperatures of 85˚C measured by maximum power point tracking (MPPT).(*28*)

Currently, the main device architectures investigated in PSCs are the mesoporous TiO_2-infiltrated and the planar (mesoporous-free) configuration. Recently, we have shown that planar MA/FA, Br/I perovskites using an atomic layer deposited (ALD) SnOx electron selective layer yield stabilized efficiencies of 19.5%.(*29, 30*) The low-temperature processing enabled a monolithic silicon/perovskite tandem device with a perovskite top-cell

View Article Online
DOI: 10.1039/C7EE02901B

processed on a temperature sensitive silicon bottom-cell.(*31*) We replaced the ALD processing with a low-temperature, solution-processed deposition of SnOx resulting in efficiencies of close to 21% putting the planar architecture on par with the mesoporous counterpart.(*32*) More recently, planar PSCs with a modified low-temperature TiO_2 also achieved efficiencies of around 21%.(*33*) Even though solution-processing of metal oxides is useful for single-junction device upscaling, ALD is an ideal technique for manufacturing tandem devices(*31, 34*) involving perovskites which are sensitive to polar solvents.

One of the roadblocks limiting overall efficiency is the open-circuit voltage (V_{OC}), which can be improved by more conformal charge selective and photoactive layers.(*29-31, 35-37*) In addition, it has been shown that improving the perovskite crystal quality can also lead to improved V_{OC} and therefore higher efficiencies.(*7, 28*) Crystal impurities are commonly found in FA-based perovskites where the more bulky cations tend to partially form a wide bandgap, layered "yellow" phase polymorph (∂-$FAPbI_3$).

Here, we report on the suppression of hysteresis and the enhancement of carrier lifetimes and V_{OC} due to phase impurity management. We suppress the ∂-$FAPbI_3$ by adding only 1% of RbI to the precursor solution used to fabricate a mixed MA/FA/Pb/I/Br formulation that has reached efficiencies exceeding 18% for planar devices.(*30*) This leads to improved carrier mobility, as measured by terahertz (THz) photoconductivity. In addition, Rb-containing samples show remarkable charge carrier lifetimes above 1 µs, higher open-circuit voltages and low current-voltage (*J-V*) hysteresis, when compared to samples with remnants of ∂-$FAPbI_3$. A champion stabilized efficiency of 20.3% for SnOx-based planar PSCs is achieved; among the highest for this device configuration. Interestingly, the formation of photoinactive $RbPbI_3$ (when using concentrations of 10% RbI) does not influence the open-circuit voltage. Therefore, this study sheds light on the role of phase

View Article Online
DOI: 10.1039/C7EE02901B

impurities in charge carrier dynamics and device performance, which is imperative to going beyond state-of-the-art PSCs.

Results and Discussion

We investigated a mixed ion perovskite based on a precursor solution with the formula $Rb_x(MA_{0.17}FA_{0.83})_{(100-x)}Pb(I_{0.83}Br_{0.17})_3$, and added RbI from 1% to 10%. For brevity, we denote these compositions as Rb_xMAFA (*x* is a percentage of RbI added in solution). All preparation details are given in the supplementary information.

Film characterization

We investigated the introduction of RbI to the perovskite solution and its effect on crystal quality. In Figure 1A and B, we show X-ray diffraction (XRD) data for Rb_xMAFA with x = 0, 1, 5, 10 mol %. All compositions exhibited a typical perovskite peak at ~14° that corresponds to the (110)/(002) orientation of the photoactive black phase of the perovskite material. For MAFA additional peaks were found at 12.6° and at 11.6° corresponding to PbI_2 and (δ-$FAPbI_3$), respectively. Upon addition of small amounts of Rb from 1, 5 to 10 %, the yellow phase and the PbI_2 peaks were supressed. Similar recent reports have also shown this effect with Rb,(*38*) and others with Cs.(*7*) A small peak at 2-theta ~10° is detected for Rb-containing samples, and can be attributed to the $RbPbI_3$ compound.(*28*) More detailed XRD spectra can be found in Figure S1. Ultraviolet-visible (UV-vis) and photoluminescence (PL) spectroscopy was performed on all MAFA and Rb_xMAFA films as shown in Figure 1C. All samples showed narrow PL peaks at ~770 nm, with a small red-shift for Rb_{10}. Absorption onset also showed red shifting for the 10% Rb samples. In our recent work we showed how introduction of Rb can affect the composition

View Article Online
DOI: 10.1039/C7EE02901B

of the crystal in the bulk.(*39*) The compositional change can then lead to different bandgap formation.

The addition of the RbI in the MAFA solution leads to a lowering of the average Rb_xMAFA cation radius allowing the incorporation of cations that were considered too small previously.(*7, 28*) The black phase is entropically stabilized even at room temperature, resulting in a suppression of the hexagonal ∂-$FAPbI_3$ perovskite. With the addition of RbI, a visible black-phase perovskite is induced upon antisolvent quenching and without heat treatment (Figure 1D). RbI addition is therefore able to induce the black (cubic) perovskite crystallization without the need of heat treatment, similar to the effect of Cs.(*40*)

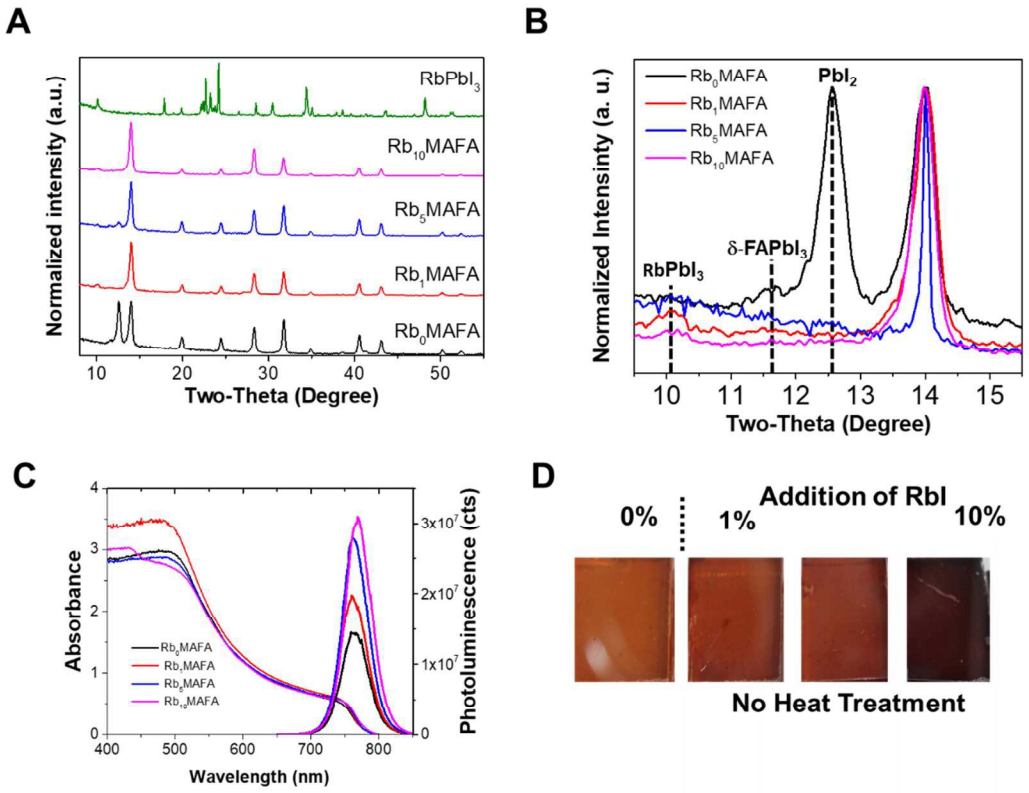

View Article Online
DOI: 10.1039/C7EE02901B

Figure 1 XRD and optical characterization of RbxMAFA compounds. A. XRD spectra for Rb_xMAFA series and the $RbPbI_3$ reference, and **B.** the 2-theta details from 9˚ to 16˚, XRD of perovskite films with the main peaks. **C.** UV-vis (line-symbol) and photoluminescence (solid lines) spectra for all samples. **D.** Photographs of samples without and with Rb addition (from left to right 0, 1, 5, 10%), and no heat treatment, to show the effect RbI addition has on crystallization at room temperature.

We investigated the morphological changes upon addition of RbI, as shown in Figure 2. Top-view scanning electron microscopy (SEM) images of perovskite films with 0, 1, 5 and 10% of Rb are shown as A, B, C and D, respectively. As the Rb content is increased, the grain size slightly increases. The MAFA composition shows a crystal size average of 307 nm distributed on the film surface. With the addition of 1% of Rb in MAFA we see an increased grain size by 70 nm to an average of 381 nm, with small crystallites embedded in larger ones, as for the MAFA controls. Addition of 5 and 10% of RbI increased average grain size to 433 and 452 nm, respectively, and small crystallites (seen in samples 0 and 1% RbI) are suppressed. The grain size change is rather small. However, it has been shown that larger grains are beneficial for charge transport and improved device performance.(*29, 36, 41*) All the grain size distributions are shown in Figure S2.

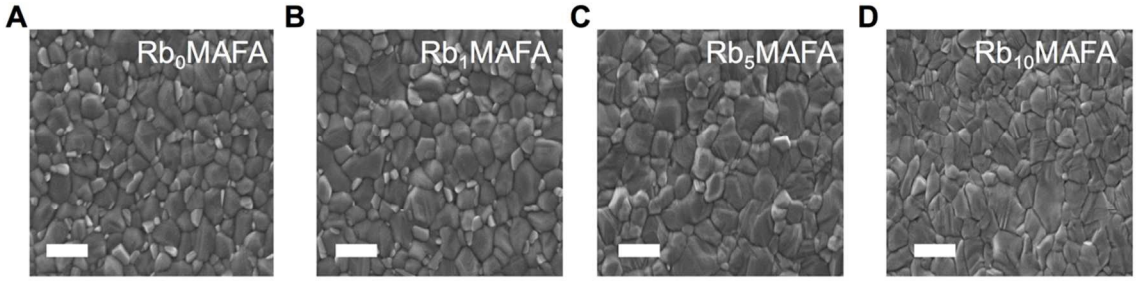

Figure 2. The effect of RbI addition on perovskite morphology. Scanning electron micrographs for perovskites based on **A.** Rb_0MAFA, **B.** Rb_1MAFA, **C.** Rb_5MAFA, and **C.** Rb_{10}MAFA, scale bar in all SEM images is 400 nm.

Solar cell performance metrics

A schematic and a cross-sectional scanning electron microscopy image of a complete solar cell is shown in Figure 3A and B, respectively. The solar cell structure used is a stack of

View Article Online
DOI: 10.1039/C7EE02901B

glass/fluorine-doped tin oxide (FTO)/SnOx/perovskite/spiro-OMeTAD/gold. Compatible with Si/perovskite tandems, the 15 nm of SnOx as the electron selective layer, is deposited by ALD. The perovskite and hole selective layers (spiro-OMeTAD) are 500 nm and 200 nm thick, respectively. An 80 nm gold layer is thermally evaporated as the top electrode.

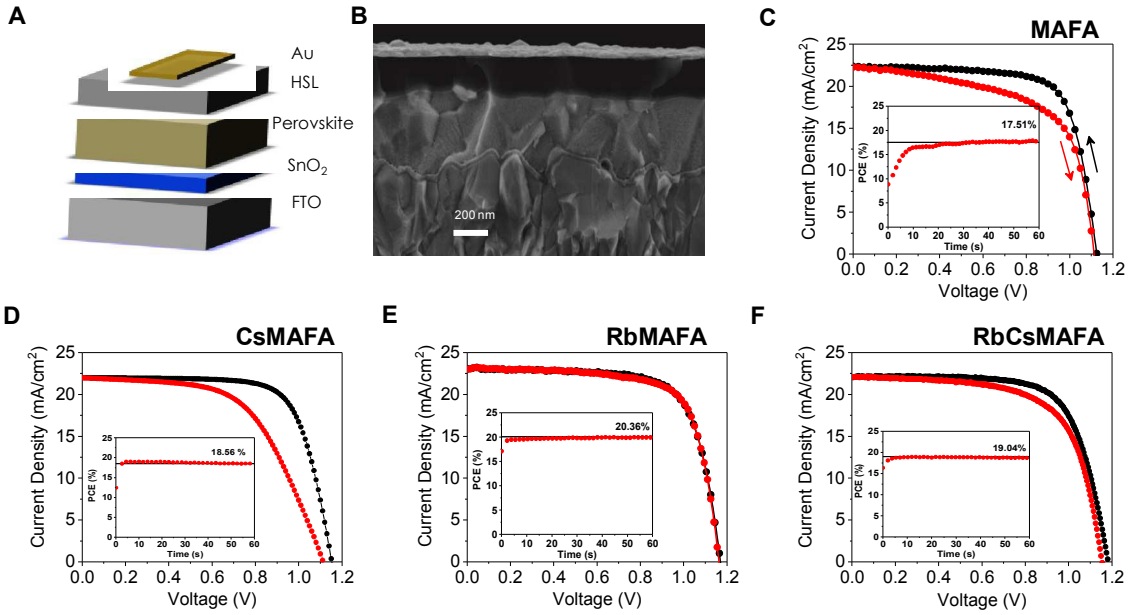

Figure 3. Performance metrics of planar perovskite solar cells based on different compositions. A. Schematic and, **B.** Cross-sectional SEM of a typical planar perovskite solar cell FTO/SnO_X/perovskite/spiro-MeOTAD/gold. **C.** Current density–voltage characteristics for a PSC without Rb or Cs, **D.** with 5% Cs in MAFA, **E.** the champion PSC with 1% of Rb in MAFA and **F.** with 5% Rb, 5% Cs in MAFA. All solar cells were measured at a scan rate of 10 mV s^{-1} and AM 1.5 G illumination with light intensity of 100 mW cm^{-2}. Insets are the maximum power point tracking for each device and an active area for each pixel of 0.16 cm^2. For statistics on all of these compositions see Figure S3 and S4.

The photovoltaic characteristics of the best PSCs for MAFA is plotted in Figure 3C, where devices yielded 17.5% by MPPT, similar to earlier reports on ALD SnOx planar PSCs with that same composition.(*30*) Large hysteresis is prevalent in the current-voltage curves. Upon addition of 5% Cs into the MAFA perovskite, the V_{OC} is increased slightly as is the efficiency, which reaches 18.5% by MPPT (Figure 3D), similar to the stabilized 19% obtained in our earlier work. Interestingly, no major difference is observed in hysteresis

View Article Online
DOI: 10.1039/C7EE02901B

with the addition of Cs. We note that we showed similar behavior in our earlier study, if slightly less hysteretic, where a combination ALD SnOx and CsMAFA also yielded relatively high hysteresis. Higher stabilized efficiencies for Rb-added samples were achieved, where the champion device yielded 20.3% for samples with 1% Rb (Figure 3E) and 19% for samples with 5% Rb and 5% Cs in the MAFA mixtures (Figure 3F).

The *J-V* characteristics for the 1% Rb show a high open circuit voltage of 1.17 V, a current density of 23.1 $mA \cdot cm^{-2}$ (using an antireflective coating) and a very low hysteresis. We note that these devices are measured 1 or 2 days after preparation. In our previous work,(*30*) we reported that in order to achieve the highest hysteresis-free efficiency, the samples were measured after 1 week or longer. Surprisingly, by adding only 1% Rb, the samples show significantly reduced hysteresis conditions without the time delay of days that is characteristic for MAFA perovskites.

While this work is based mostly on planar PSCs with SnOx selective contacts by ALD, we also prepared devices using a combination of spin-coating (SC) and chemical bath deposition (CBD), to understand the interactions of the contact and the perovskite composition.(*32*) In our previous work we used CsMAFA perovskites as the photoabsorber and here, in the attempt to understand the role of Rb in other planar PSCs, we compare both SnOx deposition methods. Similar to the Rb effect in ALD SnOx, hysteresis is significantly changed upon addition of Rb to MAFA in SC-CBD-based devices (Figure S3). One important thing to note, is that the morphology of SnOx is very different depending on deposition method. While SnOx by ALD makes a smooth and conformal layer, by SC-CBD, the layer is rougher.(*30, 32*) Moreover, as we have reported, hysteresis can be affected by time scale,(*42*) morphological features,(*36*) energetics,(*30*) and

View Article Online
DOI: 10.1039/C7EE02901B

recombination.(*43*) For that reason, we focus on the hysteresis behavior using only ALD as a highly controlled deposition technique, to avoid creating additional effects.

Photovoltaic parameters (more than 60 devices were made in total) for all compositions are shown in Figure S4. We can observe that the V_{OC}, J_{SC}, and PCE increase when adding Cs to MAFA, and further when adding Rb to the CsMAFA perovskite. The addition of Rb to MAFA sees similar response to that of RbCsMAFA, regardless of the concentration of Rb introduced (up to 10% in solution). The increase in J_{SC} can be attributed to the hysteresis effect, where scan rate can determine its magnitude, as has been shown in other works.(*29, 35, 36*) Fill factor variations are difficult to assess due to severe changes between the backward and forward scan (hysteresis effect; the dependence of FF on scan rate in Fig. 4D and E). Interestingly, the formation of wider bangap and layered $RbPbI_3$ phase is not shown to significantly change recombination dynamics, and by proxy the V_{OC}. On the other hand, the supression of PbI_2 and ∂-$FAPbI_3$ impurities allows for higher V_{OC}.

Hysteresis

To establish that Rb has such a significant effect on hysteresis and Cs alone does not, we collected over 60 device hysteresis metrics (Figure 4A), defined as the difference in efficiency between the backward and forward scan. In Figure S5, we show that although Rb concentration has a relatively small effect on the backward scan of statistically-significant device metrics, it does have a large effect on the stabilized efficiencies. This also exemplifies the need to use MPPT to measure devices, in addition to the ubiquitous J-V curve.

View Article Online
DOI: 10.1039/C7EE02901B

We investigated the transient phenomena that define hysteresis. First, we measure the effect of RbI addition on the movement of ions. Figure 4B presents the imaginary part of the current response to the intensity modulated photocurrent (IMPS) of devices with 1% and without RbI. The measurement shows that the slow component in the 0.1-100 Hz range is present for both types of devices. We attribute this to a response to light modulation which is due to ionic movement within the perovskite and it is in good agreement with our earlier work.(*36*) This slow time component is strongly tied to hysteresis and it was shown that faster response (i.e. higher frequency) to light modulation is a sign of faster equilibration currents and therefore *J-V* hysteresis is unlikely to be detected at the scan speed typically used (10 mV/s). From this analysis, devices with only 1% of RbI are expected to exhibit minimal hysteresis compared to the MAFA analogues.

We measured the effects of RbI addition to the charge carrier mobilities of the studied perovskites. We know that in PSCs, the electric field distribution is influenced by intrinsic mobile ionic defects, such as I vacancies, which tend to screen the electric field by accumulating at interfaces. Low carrier mobility causes ionic defects to respond slowly to voltage changes and are believed to be responsible for the hysteresis.(*42, 44, 45*) The hysteresis occurs because the collection efficiency of photogenerated charge carriers is dependent on the applied voltage, and on the corresponding electric field. Therefore, hysteresis can be suppressed by increasing charge carrier mobility and extraction to make it less sensitive to the electric field. (*46*) We studied the mobility of these perovskites with terahertz (THz) photoconductivity measurements. We found that charge carrier mobility increases with Rb concentration, which could also explain how devices reaches equilibrium currents faster and reduce hysteresis, as charges are collected faster than ions move. Figure

View Article Online
DOI: 10.1039/C7EE02901B

4C shows effective charge carrier mobility results from 400-nm pump THz-probe transient photoconductivity measurements.(*47*) Each 400-nm pump pulse excites n=2x10^{19} cm^{-3} carriers in all samples, as the EQE (Figure S6) and absorption do not change with RbI addition (up to 5% Rb), and we obtain effective THz mobility by dividing measured photoconductivity ($\Delta\sigma$) by elementary charge q and n. The carrier mobility for Rb_1MAFA improved by 8% with respect to Rb_0MAFA. For Rb_5MAFA, the carrier mobility increased even further by 25%, relative to Rb_0MAFA. Additionally, the increased development of a photoinactive $RbPbI_3$ phase (which appears at 1% RbI) did not seem to hinder the photoconductivity, at least up to 5% Rb. This increase in mobility could possibly be the result of increasingly larger grain size.

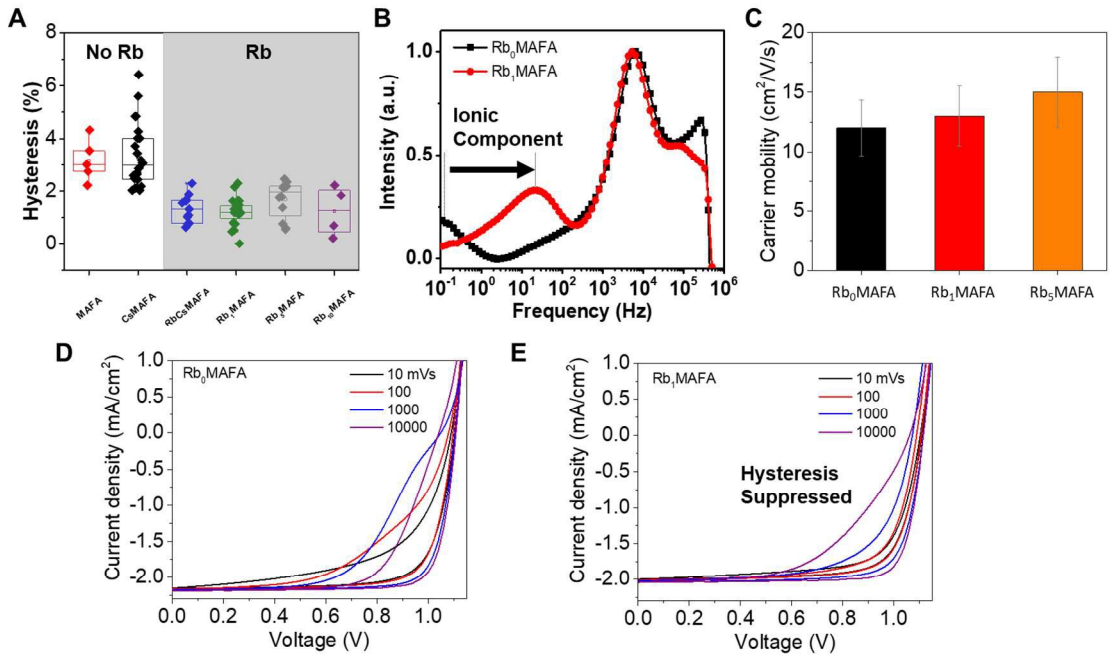

Figure 4. Study of hysteresis for devices fabricated with different perovskite compositions. A. Statistically-significant hysteresis (defined as the difference in efficiency between the backward and forward scan) for devices with different compositions. Here devices with perovskites containing Rb vs. those containing no Rb, are highlighted. **B.** Intensity modulated photocurrent spectroscopy in the imaginary part of the current response(*36*), where the low frequency feature is highlighted for its relation to ionic

View Article Online
DOI: 10.1039/C7EE02901B

movement. Current-voltage curves at different scan speeds for devices, **C.** Effective THz carrier mobility for perovskite films on quartz slides. **D.** Current-voltage plots at different scan rates without and **E.** with 1% Rb.

To further characterize and understand the changes in hysteresis we performed JV scans as a function of scan rate (Figure 4 D and E). We observe that the hysteresis increases for faster scans up to a certain scan rate before it decreases again, for the MAFA control, and it decreases regardless of scan rate for the RbMAFA device. This is consistent with previous studies, which explained this behavior with a characteristic response time of the slowly moving ions.(*42*) Both, MAFA (Figure 4D) and Rb_1MAFA (Figure 4E) devices show this trend, however on different time scales. Hysteresis is similarly pronounced for both systems when the scan is performed at 10 to 100 mV/s for MAFA and at 10,000 mV/s for Rb_1MAFA. This implies a response that is two to three orders of magnitude faster for the Rb_1MAFA device, matching the results from IMPS (Figure 4B). This trend in response time is also reflected in current transients obtained upon a voltage step from 0 or 1.15 V prebias to 1 V (Figure S7). Interestingly, instantaneously after switching the voltage from 0 to 1 V, the photocurrent is similarly low (almost 0), indicating that the ion distribution that was established at 0 V prebias affects both devices in the same way. However, the Rb_1MAFA device reaches equilibrium currents much faster. Therefore, we conclude that addition of RbI, suppression of impurity phases and slightly larger grains allow for a fast redistribution of the ions and avoid unfavorable trapping of ionic charge, aided by the increase in mobility (Figure 4C). This reduces hysteresis and allows for higher values of stabilized power.

Non-radiative recombination

View Article Online
DOI: 10.1039/C7EE02901B

With the addition of 1% or more RbI to the MAFA perovskite, a systematic increase in V_{OC} was achieved. Figure 5A shows the average and maximum V_{OC} achieved for MAFA, 1%, 5%, and 10% RbI samples. With as little as 1% RbI, V_{OC} increased by 15-20 mV. In Figure 5B, all batches made with RbI showed higher V_{OC}'s compared with the MAFA controls, hinting at reduced non-radiative recombination. We performed time resolved photoluminescence (TRPL) studies to investigate the dynamics of recombination through lifetime of photoexcited carriers in the different materials (Figure 5C). All compositions with RbI showed a long exponential PL decay tail with time constants above 1 µs, contrasting the short-lived traces for the MAFA reference yielding 0.55 µs (Table 1). This is in agreement with the higher voltages shown in Figure 5A and B for the RbI-added samples. In addition to the increased lifetimes, we observed an increase in the number of detected photons, which is directly related to the radiative quantum yields of these materials, by a factor of 4, 12 and 17 for Rb_1MAFA, Rb_5MAFA, Rb_{10}MAFA, respectively, when compared to Rb_0MAFA (Table 1). Interestingly, the initial fast decay seems to follow a different trend. Samples with 1% RbI show a decrease of the quenched early time component, suggesting a more defect-free material than the original neat MAFA. This trend is reversed as RbI concentration is increased to 10% leading to further increase of quenching in this faster regime, without affecting the long-tail component. However, these early time dynamics do not appear to affect the V_{OC} of the full devices significantly. We hypothesize that the δ-$FAPbI_3$ is recombination active and drives the V_{OC} down whereas the formation of the $RbPbI_3$ phase (from XRD in Figure 1) does not affect recombination significantly to dominate the change in V_{OC}.

View Article Online
DOI: 10.1039/C7EE02901B

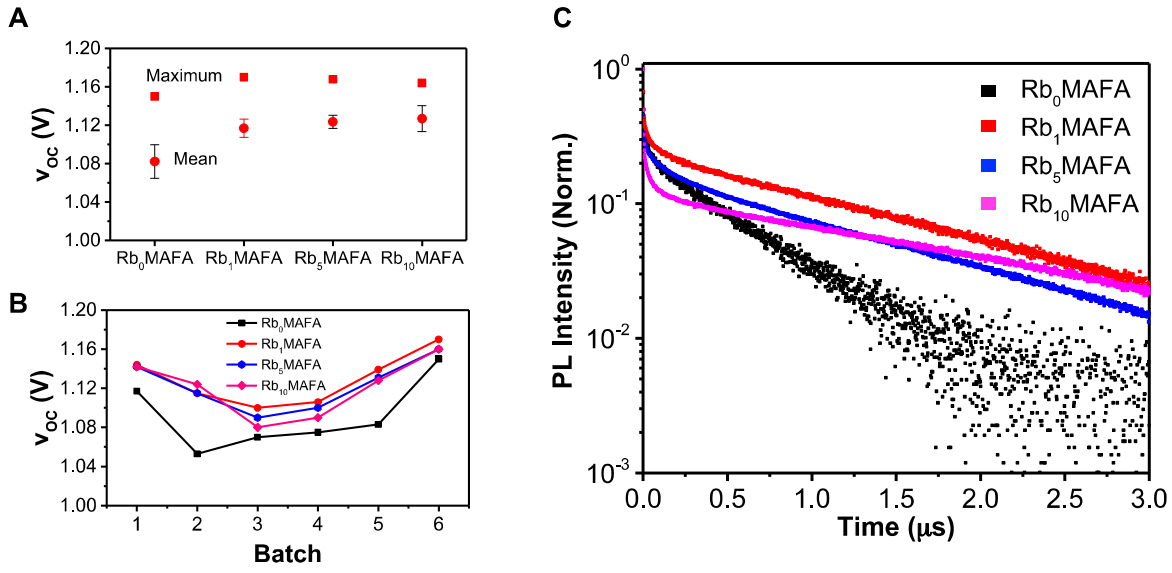

Figure 5 Open-circuit voltage and charge carrier lifetimes A. Average V_{OC} for Rb_0MAFA, Rb_1MAFA, Rb_5MAFA and $Rb_{10}MAFA$ and respective **B.** V_{OC} over six batches. **C.** Time-resolved photoluminescence lifetimes for perovskite films on glass slides (measured through the glass side to avoid emission from air-exposed layers).

Table 1. Relative yields (counts) and charge carrier lifetimes. Data extracted from the TRPL lifetimes in Figure 5C. The lifetimes are extracted from the long-tail of the traces.

Sample	Total Counts	Lifetime (µs)
Rb_0MAFA	1.48E+06	0.55
Rb_1MAFA	6.35E+06	1.37
Rb_5MAFA	1.79E+07	1.30
$Rb_{10}MAFA$	2.56E+07	1.93

Conclusions

We have investigated the effects of RbI incorporation into a mixed ion perovskite solution containing $FAPbI_3$ and $MAPbBr_3$ (precursor solution composition of 83% and 17%, respectively). Addition of as little as 1% RbI in precursor solution, suppressed the yellow phase characteristic of $FAPbI_3$, and the excess PbI_2 found in the films. These improvements

View Article Online
DOI: 10.1039/C7EE02901B

in the polycrystalline films led to significantly lower hysteresis for the Rb-containing films and higher stabilized efficiencies up to 20.35% for the 1% RbI samples. The mobility of the films was increased significantly, which we believe is instrumental for the suppression of hysteresis. In addition, the incorporation of RbI yielded longer charge carrier lifetimes and systematically higher V_{OC}'s. This work represents an important advancement in understanding and supressing hysteresis to ultimately achieve planar perovskite solar cells beyond 21%.

Materials and Methods

Materials

All materials were purchased from Sigma-Aldrich and used as received, unless stated otherwise. The organic cation iodide salts were purchased from Dyesol; the lead compounds from TCI and the RbI from abcr GmbH.

Lead halide perovskite precursor solutions

MA/FA perovskite: The "mixed" perovskite precursor solutions are composed of a mixed ion recipe reported earlier.(*30*) The precursor solution contains FAI (1 M), PbI_2 (1.1 M), MABr (0.2 M) and $PbBr_2$ (0.22 M) in anhydrous DMF:DMSO 4:1 (v:v).

Rb/MA/FA perovskite: Then 1.5 M stock solution of RbI (abcr GmbH) in DMSO was added to above solution (MA/FA perovskite) in the following volume ratios: 1:99, 5:95 and 10:90, which is described in the text as 1%, 5% and 10%, respectively.

Solar cell Preparation

Glass preparation: F:SnO_2 (FTO) substrates (NSG-10) were chemically etched with zinc powder and 4 M HCl solution and then cleaned through immersing in piranha solution (H_2SO_4/H_2O_2 = 3:1) for 10 min. All substrates were further cleaned by UV-ozone for 15 min before deposition of SnO_2.
Preparation of SnO_2 by ALD: SnO_2 control planar devices were deposited through atomic layer deposition of Tetrakis(dimethylamino)tin(IV) (TDMASn, 99.99%-Sn, Strem Chemicals INC, heated at 55 °C) and ozone in a Savannah ALD 100 instrument (Cambridge Nanotech Inc.), at 118 °C. Oxygen gas (99.9995% pure, Carbagas) was used for production of ozone (13% in O_2) by a generator (AC-2025, IN USA Incorporated). the carrier gas was Nitrogen (99.9999% pure, Carbagas) with a flow rate of 10 sccm. The growth rate (0.065 nm/cycle) was measured by ellipsometry.
Preparation of SnO_2 by CBD: 0.5 g urea were dissolved in 40 mL deionized water, followed by the addition of 10 µL mercaptoacetic acid and 0.5 mL HCl (37 wt%). Finally,

View Article Online
DOI: 10.1039/C7EE02901B

$SnCl_2 \cdot 2H_2O$ was dissolved in the solution at 0.002 M followed by stirring for 2 min. The deposition was made by placing the substrates vertically in a designed glass container filled with the solution in a 70 °C lab oven for 3 h.
Perovskite deposition: The perovskite solution was spin coated in a two steps program (10 s at 1000 rpm and 20 secs at 6000 rpm). During the second step, 200 µL of chlorobenzene was poured on the spinning substrate 20 s prior to the end of the program. The substrates were then annealed (at 100 °C unless stated otherwise) for 1 h in a nitrogen filled glove box.

Hole transporting layer: After the perovskite annealing, the substrates were cooled down for few minutes and a *spiro-OMeTAD* (Merck) solution (70 mM in chlorobenzene) was spin coated at 4000 rpm for 20 s. Spiro-OMeTAD was doped with bis(trifluoromethylsulfonyl)imide lithium salt (Li-TFSI, Sigma-Aldrich), tris(2-(1H-pyrazol-1-yl)-4-tert-butylpyridine)-cobalt(III)tris(bis(trifluoromethylsulfonyl)imide) (FK209, Dynamo) and 4-tert-Butylpyridine (tBP, Sigma-Aldrich). The molar ratio of additives for spiro-OMeTAD was: 0.5, 0.03 and 3.3 for Li-TFSI, FK209 and tBP respectively.

Finally, 70-80 nm of gold top electrode was thermally evaporated under high vacuum.

Characterization

The solar cells were measured using a 450 W xenon light source (Oriel). A Schott K113 Tempax filter (Präzisions Glas & Optik GmbH) was used to reduce the spectral mismatches between AM 1.5G and the light source. A Si photodiode equipped with an IR-cutoff filter (KG3, Schott) was used as a reference. Current-voltage data were obtained by applying an external voltage bias and measuring the current response with a digital source meter (Keithley 2400). The voltage scan rate was set to 10 mV s^{-1}. The photovoltaic data was collected without any device preconditioning, such as light soaking. In order to fix the active area of the devices and avoid artifacts produced by scattered light a black metal mask was used during the measurements. The IV data for champion devices gathered with antireflective coating on a 0.16 cm^2 mask aperture whereas the data for the statistical analysis devices collected without antireflective coating.

UV–vis measurements were performed on a Varian Cary 5. Scanning electron microscopy (SEM) was performed on a ZEISS Merlin HR-SEM. Secondary electron images were acquired with an EDX detector. X-ray powder diffractions (XRD) were recorded on an X'Pert MPD PRO (Panalytical) equipped with a ceramic tube (Cu anode, λ = 1.54060 Å), a secondary graphite (002) monochromator and a RTMS X'Celerator (Panalytical) in an angle range of $2\theta = 5°$ to 60°. Photoluminescence spectra were obtained with Fluorolog 322 (Horiba Jobin Ybon Ltd) with the range of wavelength from 620 nm to 850 nm by exciting at 460 nm. The samples were mounted at 60° and the emission recorded at 90° from the incident beam path.

Transient PL lifetimes were obtained by time-correlated single photon counting (TCSPC). The sample was excited by a pulsed 405 nm wavelength laser (PicoQuant LDH-C 400) at an average incident power of 40 nW at a repetition rate of 200 kHz. Excess laser scatter

View Article Online
DOI: 10.1039/C7EE02901B

was removed by a 405 notch filter, and 450 nm and 650 nm long-pass filters (ThorLabs). The emission was focused onto a silicon single-photon avalanche photodiode (Micro Photon Devices $PD-100-C0C) using reflective optics. Photon arrival times were recording using a PicoHarp 300 (PicoQuant). Charge carrier lifetimes are estimated by fitting the long-time component of the decay to a mono-exponential decay. The samples were prepared on cover microscope glass slides.

THz carrier mobility were obtained by transient terahertz photoconductivity measurements, monitoring the differences in THz transmission with and without optical excitation. Amplified femtosecond laser pulses (800-nm center wavelength, 1.7 mJ pulse energy, and 1 kHz repetition rate) were used for THz generation (1.2 THz), detection, and photoexcitation. Photoexcitation at 400 nm was generated by doubling the laser frequency with a thin beta barium borate crystal and then focused to 2-mm diameter on the sample at a fluence of 45 μJ cm^{-2}. The THz probe pulses were generated from a two-color laser-induced gas plasma and focused to 1-mm in diameter on the sample. The transmitted THz pulses were detected by electro-optic sampling with a 1.0 mm thick <110> ZnTe crystal. Photoconductivity was calculated by $\Delta\sigma = \left(\frac{1+n_{SiO_2}}{Z_0 d}\right)\left|\frac{\Delta T}{T_0}\right|$, where $n_{SiO_2} = 2.1$ was the index of refraction of the quartz substrate, $Z_0 = 377\ \Omega$ was the impedance of free space, $d = 50$ nm was the depth of the excited carriers (taken to be the absorption depth), and ΔT was the change in THz transmission amplitude relative to its initial THz transmission T_0. Effective carrier mobility μ was further obtained from $\Delta\sigma = qn\mu$, where q was elementary charge, and n was excited carrier density. For this measurement the perovskite solution was deposited on quartz.

Acknowledgement

L.N. was supported as part of the Center for Excitonics, an Energy Frontier Research Center funded by the US Department of Energy, Office of Science, Office of Basic Energy Sciences under Award Number DE-SC0001088 (MIT). M. S. acknowledges the support from the co-funded Marie Skłodowska Curie fellowship, H2020 Grant agreement no. 665667. MG and MS acknowledge financial support from the European Union's Horizon 2020 research and innovation program under grant agreement No 687008 (GOTSolar).

References

1. H. J. Snaith, Perovskites: The Emergence of a New Era for Low-Cost, High-Efficiency Solar Cells. *J Phys Chem Lett* **4**, 3623-3630 (2013).
2. N. Pellet *et al.*, Mixed-organic-cation perovskite photovoltaics for enhanced solar-light harvesting. *Angew Chem Int Ed Engl* **53**, 3151-3157 (2014).
3. G. E. Eperon *et al.*, Formamidinium lead trihalide: a broadly tunable perovskite for efficient planar heterojunction solar cells. *Energ Environ Sci* **7**, 982-988 (2014).
4. N. J. Jeon *et al.*, Compositional engineering of perovskite materials for high-performance solar cells. *Nature* **517**, 476-480 (2015).
5. C. Yi *et al.*, Entropic stabilization of mixed A-cation ABX3metal halide perovskites for high performance perovskite solar cells. *Energy Environ. Sci.* **9**, 656-662 (2016).
6. J. W. Lee, D. J. Seol, A. N. Cho, N. G. Park, High-efficiency perovskite solar cells based on the black polymorph of HC(NH2)2 PbI3. *Advanced materials* **26**, 4991-4998 (2014).

View Article Online
DOI: 10.1039/C7EE02901B

7. M. Saliba *et al.*, Cesium-containing triple cation perovskite solar cells: improved stability, reproducibility and high efficiency. *Energy Environ Sci* **9**, 1989-1997 (2016).
8. M. M. Lee, J. Teuscher, T. Miyasaka, T. N. Murakami, H. J. Snaith, Efficient hybrid solar cells based on meso-superstructured organometal halide perovskites. *Science* **338**, 643-647 (2012).
9. H. S. Kim *et al.*, Lead iodide perovskite sensitized all-solid-state submicron thin film mesoscopic solar cell with efficiency exceeding 9%. *Sci Rep* **2**, 591 (2012).
10. F. Hao, C. C. Stoumpos, D. H. Cao, R. P. H. Chang, M. G. Kanatzidis, Lead-free solid-state organic-inorganic halide perovskite solar cells. *Nature Photonics* **8**, 489-494 (2014).
11. J. H. Noh, S. H. Im, J. H. Heo, T. N. Mandal, S. I. Seok, Chemical management for colorful, efficient, and stable inorganic-organic hybrid nanostructured solar cells. *Nano Lett* **13**, 1764-1769 (2013).
12. S. De Wolf *et al.*, Organometallic Halide Perovskites: Sharp Optical Absorption Edge and Its Relation to Photovoltaic Performance. *J Phys Chem Lett* **5**, 1035-1039 (2014).
13. S. D. Stranks *et al.*, Electron-hole diffusion lengths exceeding 1 micrometer in an organometal trihalide perovskite absorber. *Science* **342**, 341-344 (2013).
14. G. Xing *et al.*, Long-range balanced electron- and hole-transport lengths in organic-inorganic CH3NH3PbI3. *Science* **342**, 344-347 (2013).
15. A. Kojima, K. Teshima, Y. Shirai, T. Miyasaka, Organometal halide perovskites as visible-light sensitizers for photovoltaic cells. *J Am Chem Soc* **131**, 6050-6051 (2009).
16. M. A. Green *et al.*, Solar cell efficiency tables (version 49). *Progress in Photovoltaics: Research and Applications* **25**, 3-13 (2017).
17. W. S. Yang *et al.*, Iodide management in formamidinium-lead-halide–based perovskite layers for efficient solar cells. *Science* **356**, 1376-1379 (2017).
18. N. chart, http://www.nrel.gov/ncpv/images/efficiency_chart.jpg. (2016).
19. J.-P. Correa-Baena *et al.*, The rapid evolution of highly efficient perovskite solar cells. *Energ Environ Sci* **10**, 710-727 (2017).
20. J. Burschka *et al.*, Sequential deposition as a route to high-performance perovskite-sensitized solar cells. *Nature* **499**, 316-319 (2013).
21. Z. G. Xiao *et al.*, Efficient, high yield perovskite photovoltaic devices grown by interdiffusion of solution-processed precursor stacking layers. *Energ Environ Sci* **7**, 2619-2623 (2014).
22. B. R. Li *et al.*, Chlorobenzene vapor assistant annealing method for fabricating high quality perovskite films. *Org Electron* **34**, 97-103 (2016).
23. X. Li *et al.*, A vacuum flash-assisted solution process for high-efficiency large-area perovskite solar cells. *Science* **353**, 58-62 (2016).
24. H. Choi *et al.*, Cesium-doped methylammonium lead iodide perovskite light absorber for hybrid solar cells. *Nano Energy* **7**, 80-85 (2014).
25. J. W. Lee *et al.*, Formamidinium and Cesium Hybridization for Photo- and Moisture-Stable Perovskite Solar Cell. *Adv Energy Mater* **5**, (2015).
26. C. Y. Yi *et al.*, Entropic stabilization of mixed A-cation ABX(3) metal halide perovskites for high performance perovskite solar cells. *Energ Environ Sci* **9**, 656-662 (2016).
27. Z. Li *et al.*, Stabilizing Perovskite Structures by Tuning Tolerance Factor: Formation of Formamidinium and Cesium Lead Iodide Solid-State Alloys. *Chem Mater* **28**, 284-292 (2016).
28. M. Saliba *et al.*, Incorporation of rubidium cations into perovskite solar cells improves photovoltaic performance. *Science* **354**, 206-209 (2016).

View Article Online
DOI: 10.1039/C7EE02901B

29. J. Y. Seo *et al.*, Ionic Liquid Control Crystal Growth to Enhance Planar Perovskite Solar Cells Efficiency. *Adv Energy Mater* **6**, 1600767 (2016).
30. J. P. Correa Baena *et al.*, Highly efficient planar perovskite solar cells through band alignment engineering. *Energ Environ Sci* **8**, 2928-2934 (2015).
31. S. Albrecht *et al.*, Monolithic perovskite/silicon-heterojunction tandem solar cells processed at low temperature. *Energ Environ Sci*, (2016).
32. E. H. Anaraki *et al.*, Highly efficient and stable planar perovskite solar cells by solution-processed tin oxide. *Energ Environ Sci* **9**, 3128-3134 (2016).
33. H. Tan *et al.*, Efficient and stable solution-processed planar perovskite solar cells via contact passivation. *Science* **355**, 722-726 (2017).
34. K. A. Bush *et al.*, 23.6%-efficient monolithic perovskite/silicon tandem solar cells with improved stability. *Nature Energy* **2**, 17009 (2017).
35. M. Hadadian *et al.*, Enhancing Efficiency of Perovskite Solar Cells via N-doped Graphene: Crystal Modification and Surface Passivation. *Advanced materials* **28**, 8681-8686 (2016).
36. J. P. Correa-Baena *et al.*, Unbroken Perovskite: Interplay of Morphology, Electro-optical Properties, and Ionic Movement. *Advanced materials* **28**, 5031-5037 (2016).
37. W. Nie *et al.*, Solar cells. High-efficiency solution-processed perovskite solar cells with millimeter-scale grains. *Science* **347**, 522-525 (2015).
38. T. Duong *et al.*, Structural engineering using rubidium iodide as a dopant under excess lead iodide conditions for high efficiency and stable perovskites. *Nano Energy* **30**, 330-340 (2016).
39. B. Philippe *et al.*, Chemical distribution of multiple cation (Rb+, Cs+,MA+, FA+) perovskite materials by photoelectron spectroscopy. *Chem Mater*, (2017).
40. T. Matsui, J. Y. Seo, M. Saliba, S. M. Zakeeruddin, M. Gratzel, Room-Temperature Formation of Highly Crystalline Multication Perovskites for Efficient, Low-Cost Solar Cells. *Advanced materials*, 1606258-n/a (2017).
41. Y. C. Shao *et al.*, Grain boundary dominated ion migration in polycrystalline organic-inorganic halide perovskite films. *Energ Environ Sci* **9**, 1752-1759 (2016).
42. W. Tress *et al.*, Understanding the rate-dependent J-V hysteresis, slow time component, and aging in CH3NH3PbI3 perovskite solar cells: the role of a compensated electric field. *Energ Environ Sci* **8**, 995-1004 (2015).
43. W. Tress, J. P. C. Baena, M. Saliba, A. Abate, M. Graetzel, Inverted Current-Voltage Hysteresis in Mixed Perovskite Solar Cells: Polarization, Energy Barriers, and Defect Recombination. *Adv Energy Mater* **6**, n/a-n/a (2016).
44. V. D'Innocenzo *et al.*, Excitons versus free charges in organo-lead tri-halide perovskites. *Nat Commun* **5**, (2014).
45. E. L. Unger *et al.*, Hysteresis and transient behavior in current-voltage measurements of hybrid-perovskite absorber solar cells. *Energy & Environmental Science* **7**, 3690-3698 (2014).
46. W. Tress, Metal Halide Perovskites as Mixed Electronic–Ionic Conductors: Challenges and Opportunities—From Hysteresis to Memristivity. *The Journal of Physical Chemistry Letters* **8**, 3106-3114 (2017).
47. M.-J. Sher *et al.*, Picosecond carrier recombination dynamics in chalcogen-hyperdoped silicon. *Applied Physics Letters* **105**, 053905 (2014).

View Article Online
DOI: 10.1039/C7EE02901B

Perovskite-based solar cells have emerged as a promising technology for highly efficient and low-cost photovoltaics. High efficiencies so far reported go beyond 20% in mesoporous-based solar cells, but very few reports have shown this for the planar-based analogues. This is in part because planar perovskite solar cells have traditionally suffered from more pronounced hysteresis, detrimental to stabilized power output. In this work, we show that by improving the charge carrier mobilities and lifetimes, hysteresis is suppressed and open circuit voltages are improved. This translates into planar perovskite solar cells processed at low temperature and yielding efficiencies beyond 20%. This study sheds light on the importance of charge carrier mobility related to hysteresis, and therefore sets a pathway towards high efficiency planar perovskite solar cells.